

Snapshot dual-band visible hyperspectral imaging spectrometer

John Hartke, MEMBER SPIE
United States Military Academy
Photonic Research Center
West Point, New York 10996
E-mail: john.hartke@usma.edu

Eustace L. Dereniak, FELLOW SPIE
University of Arizona
College of Optical Sciences
Tucson, Arizona 85721
E-mail: eustace@optics.arizona.edu

Abstract. We describe a proof of concept for a snapshot dual-band visible hyperspectral imaging spectrometer. A commercially available digital camera was integrated into a computed tomographic imaging spectrometer to provide a means for this proof of concept. Two spatially coregistered data cubes covering the blue (400 to 500 nm) and red (600 to 700 nm) spectral regions were reconstructed and the results analyzed. We found that the system accurately reconstructs the spectral content of the scene and that the two data cubes are automatically spatially coregistered by virtue of the system design. © 2007 Society of Photo-Optical Instrumentation Engineers. [DOI: 10.1117/1.2434348]

Subject terms: Dual band; hyperspectral imaging; imaging spectrometer; computed tomographic imaging spectrometer.

Paper 060189R received Mar. 21, 2006; revised manuscript received Jun. 13, 2006; accepted for publication Jun. 16, 2006; published online Jan. 26, 2007. This paper is a revision of a paper presented at the SPIE conference on Infrared Systems and photoelectronic Technology, Denver, Colorado, Apr. 2004. The paper presented there appears (unrefereed) in SPIE proceedings vol. 5563.

1 Background

1.1 Imaging Spectrometer

Imaging spectrometry involves the acquisition of the spatially registered spectral content of a scene of interest. The manifestation of an imaging spectrometer is the creation of a data cube. A data cube is a three-dimensional representation of the scene with two spatial coordinates and one wavelength coordinate (x, y, λ) . The value at each three-dimensional point within the data cube is a radiometric measurement in spectral irradiance. We define the three-dimensional volume element $(\Delta x, \Delta y, \Delta \lambda)$ within the data cube as the *voxel*. The voxel size limits the spatial and spectral resolution of the system. Using the data cube as a representation of the scene allows for spectral analysis of the scene. Slices in the data cube along a constant wavelength provide a monochromatic image of the scene, whereas a spatial location in the data cube at a particular (x, y) coordinate provides the spectral signature of the object at that coordinate.

There are several instances where we have a need to investigate two separate spectral regions of the same scene. For example, we may be interested in the mid (3 to 5 μm) and long (8 to 12 μm) wave infrared atmospheric transmission windows. By analyzing both spectrums simultaneously, we can increase our ability to detect targets in clutter and distinguish between targets and decoys.¹ Nearly every application of dual-band imaging spectrometry has the same goal: to provide the spatial coregistered spectral content of the scene over two separate spectral bands.

Historical means of imaging spectrometry include whisk broom, push broom, and filter wheel systems. A whisk broom imaging spectrometer uses a diffraction grating in front of a line of detectors. The diffraction grating spreads

the spectral content of the very narrow field of view along the line of detectors. The system then sweeps back and forth across the scene of interest as the detectors move forward until the entire scene is covered. The push broom system is similar to the whisk broom system in that a diffraction grating disperses the spectral content of the scene along a line, but in this case there is a two-dimensional array of detectors behind the grating. This system captures the spectral content of the x coordinates of the data cube while the system scans along the y coordinates. The filter wheel system consists of a conventional camera system that takes an image of the entire field of view but has a very narrow band spectral filter in front of the detector array. The filter is repeatedly changed until each monochromatic plane of the data cube is filled in. In each of these cases, it takes several integration times to completely fill the data cube.

1.2 Computed Tomographic Imaging Spectrometer

Given the advances in computing power, another type of imaging spectrometer, the computed tomographic imaging spectrometer (CTIS), has been proven effective for completing the data cube with a single integration time and no moving parts.² The CTIS optical system consists of four main optical elements: objective optics, collimating optics, a disperser, and a reimaging element. The objective takes the scene and images it to the field stop. The collimator takes the light from the field stop and collimates it to pass through the computer generated holographic (CGH) disperser. After passing through the disperser, the light is reimaged to a two-dimensional detector array (Fig. 1).³

The CTIS system is based on the computed tomographic techniques similar to those used in medical imaging. Computed tomography involves reconstructing a three-dimensional data cube from a series of two-dimensional projections of the object. In this system, the two-

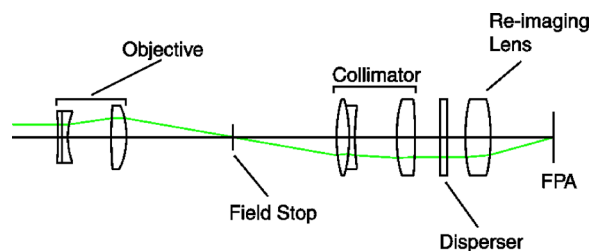


Fig. 1 Schematic of a CTIS system.

dimensional projections are created by the dispersive CGH element in the collimated space of the system. The two-dimensional projections are the diffracted images of the object's image in the plane of the field stop and constitute a series of parallel projections of the three-dimensional object cube.⁴ The center, or zero order projection, is a direct polychromatic image of the image in the field stop. The higher diffraction orders are projections through the data cube at different angles measured from the wavelength axis.

Key to the CTIS system is the dispersive element. The system in this research uses a CGH etched phase grating. The CGH for this system was made from polymethylmethacrylate (PMMA) material etched with an electron beam. The dispersion of the light is achieved by changing the depth of the PMMA and thus changing the phase of the wave front at each point. The phase imparted to the plane wave by the CGH is given by

$$\Phi = \frac{2\pi d}{\lambda}(n - 1). \quad (1)$$

Here Φ is the imparted phase, d is the etch depth of the material, λ is the wavelength of the light, and n is the index of refraction of the PMMA.

The disperser is composed of numerous unit cells. Each cell consists of an integer number (usually 8×8 , 10×10 , or 16×16) of square phasels. Each phasel is etched to a specified depth. The term *phasels* is used to distinguish the cell etching of the CGH from the detector pixel on the focal plane array and the *voxel*, which is the three-dimensional unit cell of the data cube. The etched depth leads to a phase

delay of the transmitted wave front. The number of phasels in a unit cell and the number of unit cells on the CGH are design parameters.

The phase imparted to the wave front by the CGH creates the tomographic projections through the data cube. CGHs can be designed to create one of several different two-dimensional diffraction patterns. A 3×3 diffraction pattern consists of the central zero order with first order diffraction orders in the horizontal and vertical directions as well as the diagonals to fill the square pattern. Figure 2 is an example of the image created by a 7×7 CGH disperser. When choosing a design for a CGH, we must consider the required spectral and spatial resolution, focal plane characteristics, and the object's characteristics. The zero order size influences the spatial resolution of the system and the dispersion of the outermost diffraction order influences the possible spectral resolution.

The computed tomographic reconstruction techniques used to reconstruct the data cube are expectation maximization (EM) and multiplicative algebraic reconstruction technique (MART). For both reconstruction algorithms, we model the CTIS system with the equation

$$\mathbf{g} = \mathbf{H}\mathbf{f} \quad (2)$$

where \mathbf{g} is the image vector obtained from the focal plane, \mathbf{H} is the two-dimensional system matrix, and \mathbf{f} is the object vector. The reconstructions attempt to estimate \mathbf{f} given the \mathbf{H} matrix and the image vector \mathbf{g} . The size of the \mathbf{H} matrix prevents the use of singular valued decomposition to solve for \mathbf{f} .

The EM algorithm for reconstruction is rooted in Poisson statistics. We start by assuming that the CTIS system has signal-dependent photon noise dominating the system. We then look for an estimate of the object $\hat{\mathbf{f}}$ that maximizes the probability of the measured image or maximizes $P(\mathbf{g}|\hat{\mathbf{f}})$. This leads to the following iterative process for the reconstruction:

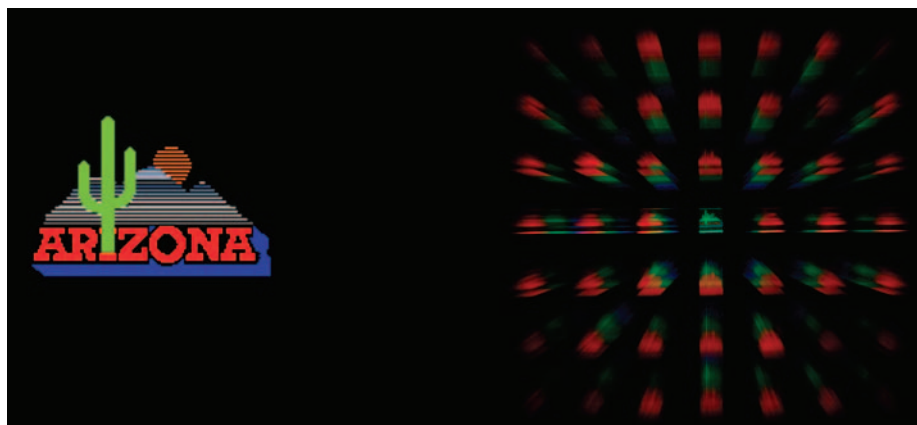


Fig. 2 Diffraction pattern created by a 7×7 CGH disperser (b) of the object (a).

$$\hat{f}_n^{(k+1)} = \frac{\hat{f}_n^{(k)}}{\sum_{m'=1}^M \mathbf{H}_{m'n}} \sum_{m=1}^M \mathbf{H}_{mn} \frac{g_m}{(\mathbf{H}\hat{f}^{(k)})_m}. \quad (3)$$

Here k is the iteration number, m denotes the m 'th component of \mathbf{g} , and n is the n 'th component of \mathbf{f} . We can now use Eq. (3) repeatedly until the changes in \hat{f}_n from one iteration to the next is small enough, or until we start to see noise amplification.⁵

The advantages of the EM algorithm are that it has a rapid, nonlinear convergence and that each iteration is, in general, a better estimate than the last. The drawback of the EM algorithm is that it has a tendency to produce high frequency spatial and spectral features, especially near the edges of the data cube.⁶

MART is based on finding a maximum entropy reconstruction. Entropy in this context is defined as

$$S = - \sum_{n=1}^N f_n \ln f_n, \quad (4)$$

where n is the n 'th component of \mathbf{f} .

The assumptions needed to apply MART are that \mathbf{g} , \mathbf{H} , and \mathbf{f} are all nonnegative and the elements of \mathbf{H} are scaled to be less than or equal to 1.⁷ The iterative algorithm used to reconstruct the estimated data cube is⁸

$$\hat{f}_n^{(k+1)} = \left(\frac{\mathbf{H}^T \mathbf{g}}{\mathbf{H}^T \mathbf{H} \hat{f}^{(k)}} \right) \hat{f}_n^{(k)}. \quad (5)$$

The advantages of the MART method are that it converges very quickly and the reconstruction of high frequency objects is smoother, which reduces the high frequency spikes present in other reconstruction algorithms.⁹ It can be advantageous to apply the MART algorithm to the estimate obtained from the EM algorithm to smooth out the high frequency artifacts created by the EM iterations.

The advantage of the CTIS over the scanning techniques of the whisk broom, push broom, or filter wheel is that the CTIS can capture all the information required to reconstruct the data cube of a dynamic scene in a single snapshot. The other systems need to use numerous snapshots to acquire the same information. If the scene is changing very rapidly, the scanning techniques may not have completed the data cube capture prior to scene change.

One of the disadvantages of the CTIS system and the spatial scanning systems, such as whisk broom and push broom, is that the diffracting optical elements that spread the spectral content of the scene over the focal plane are limited to one spectral octave. The one octave spectral limit is due the fact that the constructive interference from integer multiples of the wavelength will occur at the same point on the detector array as the diffraction order increases. As an example, we expect the second diffraction order of 1- μm light to fall in the exact same point on the detector array as the first diffraction order of 2- μm light. The result of this order overlap is that we cannot tell whether the detector reading at that point is due to 1- or 2- μm light.

The order overlap problem is exacerbated when we consider a dual-band imaging spectrometer. If we again con-

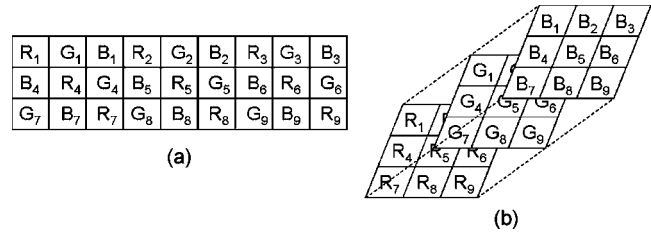


Fig. 3 Interwoven focal plane design (a) output results in three two-dimensional arrays, one for each color (b). Here the letters R , G , and B correspond to pixels sensitive to the red green and blue portions of the visible spectrum. The numeric subscript gives the pixel location in the output array vector.

sider the mid and long wave infrared atmospheric transmission windows, half of the second order mid (4 to 5 μm) wave band overlaps most of the first order of the long (8 to 10 μm) wave band. A possible solution to the order overlap problem is to split the incoming light onto two separate focal planes and analyze them independently. The issue with this technique is that it becomes very difficult to coregister the spatial information of each focal plane. It is possible to resolve the order overlap problem and the spatial coregistration problem if the focal plane array consists of a mix of detectors that are in an interwoven pattern sensitive to the different spectral bands of interest such as the dual-band technology recently developed.¹⁰

2 Dual-Band Solution

It is possible to overcome the order overlap limitation and maintain spatial coregistration of the data cubes by using an interwoven mixed spectral detector focal plane instead of a focal plane made up of only one spectral band detector type. Many standard digital camera focal plane arrays consist of the required interwoven mixed detectors in the visible portion of the spectrum. These focal plane arrays consist predominately of silicon detectors with filters that have three spectral bandpasses: red (600 to 700 nm), green (500 to 600 nm), and blue (400 to 500 nm). An interwoven mixed pattern of detectors is one where the detector types alternate between red, green, and blue sensitive pixels. The standard tagged image file format (TIFF) output from such a focal plane array consists of two-dimensional arrays for each color (Fig. 3). Each color array is spatially coregistered with each of the other two color arrays except that each is displaced by one pixel. Then by reconstructing data cubes from each of the individual color arrays, we have spatially coregistered data cubes with a correctable displacement, covering the red, green, and blue spectral bands of visible cameras.

3 Proof of Concept

To demonstrate the viability of the dual-band system, we conducted two experiments. The first experiment was designed to demonstrate that it is possible to reconstruct two data cubes that are spatially coregistered and to examine the spatial resolution of the system. The second experiment was designed to determine the spectral resolution of the system in both spectral bands. The spectral bands we used were blue (400 to 500 nm) and red (600 to 700 nm). We ignored the green band (500 to 600 nm) in this work.

To test the spatial characteristic of the dual-band system, we illuminated a series of black and white bars, and red and blue bars as the object. We used two different spacings between the bars in the object to characterize the spatial reconstruction. We reconstructed the data cube using MART and EM algorithms. The red and blue bars demonstrate the separability of objects with spectral components in only one band while the black and white bars demonstrate separability of objects with spectral components in both bands. We determined the spatial resolution of the system by examining the reconstruction of the object along a horizontal line. We can also check the spatial colocation of the bands by identifying the location of spatial features in both bands. For the black and white bars, we expect that the maximums occur in the same locations for both bands. For the blue and red bars, we expect that the maximum in the blue band will fall in the minimum of the red band and vice versa.

To test the spectral characteristics of the system, we reconstructed objects with a known spectral signature and compared the known spectral signature with the reconstructed signature. We used a helium-neon laser to test the red band and a blue light-emitting diode to test the blue band. We used an Ocean Optics spectrometer to obtain the spectral signature for comparison.

4 Experimental Setup

The camera used in this proof of concept is a Fuji FinePix S1 Pro digital camera. The CGH is a 7×7 disperser designed for 440 to 740 nm with a 0.75-in. clear aperture. The camera output format used was TIFF-RGB with 3040×2016 pixels in each band. The focal plane array is a 23.3×15.6 mm² first generation super charge-coupled device with color filtered detectors in an interwoven pattern. The TIFF-RGB format output consists of three two-dimensional arrays corresponding in general to the red, green, and blue regions of the visible spectrum. The band-pass of each color region was measured by sending monochromatic light into the system and measuring the percentage of the light in each color region to the total light incident on the focal plane. The full width at half maximum band pass for the blue pixels was measured to be 400 to 500 nm, the green was 500 to 600 nm, and the red was 600 to 700 nm.

The camera's internal image processing mixes detector output to create the TIFF output file. The actual image processing software that maps the detector output to the TIFF output is proprietary to Fuji and unknown to us. We will model the system output as the actual focal plane array output ignoring any mixing between the spectral bands. We assume that the digital number (DN) in the (m, n) position of the red output array corresponds to the irradiance measured at a red sensitive detector at the (m, n) location of the detector array. Similarly the DN in the (m, n) position of the blue detector corresponds to the irradiance measured at the blue sensitive detector at the (m, n) location on the detector. The assumption was tested by sending a white light point source into the system without the disperser and compared the location of response in each of the red, green, and blue arrays. We found that the white light point source was in exactly the same location and had the same spatial extent in all three arrays.

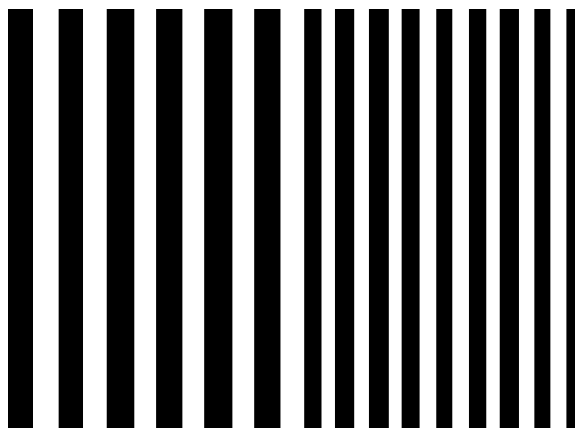


Fig. 4 Black and white bars used as spatial resolution object. The bars on the left half were 6.75-mm wide and subtended 4.4 pixels in the zero order on the focal plane. The bars on the right half were 4.75-mm wide and subtended 3.1 pixels in the zero order.

We applied eight iterations of EM to all the reconstructions. We chose EM because it was a faster reconstruction. We used eight iterations in all cases for consistency of comparing results and because we did not see changes between the seventh, eighth, or ninth iterations.

5 Results

5.1 Spatial Results

The first object was a series of black and white vertical bars (Fig. 4). The bars on the left half of the object were 6.75-mm wide, while the bars on the right half of the object were 4.75-mm wide. The second object was a series of alternating red and blue bars in the same design as the first object. Both objects were illuminated by a 75-W white light bulb. The field stop subtended an area of 105×105 pixels on the focal plane. In object space that same area was 16.2×16.2 cm. Therefore, each zero order pixel subtended an area 1.54 mm² in object space. If we assume that the spatial extent of a voxel is limited by the size of the point spread function (PSF) in the zero diffraction order of the focal plane, and that we cannot resolve objects smaller than the PSF, we can create Table 1. Table 1 shows the spatial extent of the voxel in the object plane we can resolve based on the size of the PSF in the zero order on the focal plane. We expect that to be able to resolve the larger bars of the test objects, we would need the PSF to cover an area of 5×5 pixels or less and 2×2 pixels or less for the small bars.

Figures 5 and 6 show graphs with cuts in the data cube reconstructions of the vertical bar objects in both the red and blue spectral bands. The graphs are the relative radiometric measure along a constant y pixel at a given wavelength along the x direction. From the graphs, we can draw two conclusions. The first is that the two data cubes are coregistered to within ± 2 pixels, which is within the uncertainty of the zero order spot size. The second conclusion is that the spatial resolution of the system is better than predicted by the PSF spot size.

The spatial coregistration conclusion is based on examining the locations of the peaks between the red and blue data cubes. In Fig. 5(a), the third maximum from the left in the blue bands occurs at pixel 22. In Fig. 5(b), the third

Table 1 Resolvable object size given PSF extent on focal plane.

PSF Extent (pixels)	Object Extent (mm)
1×1	1.54×1.54
2×2	3.08×3.08
3×3	4.62×4.62
4×4	6.08×6.08
5×5	7.70×7.70
6×6	9.24×9.24
7×7	10.78×10.78
8×8	12.32×12.32
9×9	13.86×13.86

peak occurs at pixel 20 in the red band. In the data cubes reconstructing the red and blue bars, we expect the peaks in the blue bands to correspond to the valleys in the red band. In Figs. 6(a) and 6(b), pixel 20 is a valley in the blue band and a peak in the red band. Combining these findings with the fact that the image of the white light point source in the zero diffraction order used during calibration is at the same (x,y) pixel location on the focal plane in both bands strengthens the conclusion that the system produces coregistered data cubes in both bands.

The spatial resolution conclusion comes from comparing the predictions in Table 1 with Figs. 5 and 6. The spot size of the zero order calibration images varied between 5×5 and 8×8 pixels. Based on Table 1, the best resolution we could expect is a 7.70-mm object. From Figs. 5 and 6, we can resolve the 6.75-mm wide bars. In many cases, we can

even resolve the 4.75-mm wide bars. An attempt to correlate the calibration spot size to spatial resolution was unsuccessful. One thing we do see that affects the spatial resolution is the noise. Figure 5 is a reconstruction of the black and white bars, while Fig. 6 is the reconstruction of the red and blue bars. The resolution is better in the black and white bar data cube than in the blue and red bar data cube. An explanation for this difference is that in the black and white case, the signal in both bands is colocated. Any cross talk between bands is seen as an increased signal in the other band. In this system, we found that when we illuminated the focal plane with a monochromatic red light source, 60% of the signal was measured in the red band and 20% each in the blue and green bands. This means that in the red and blue bar case, the 20% signal in the blue band in response to the red source is noise in the red data cube reconstruction and vice versa. Therefore the signal-to-noise ratio is higher in the black and white object than the red and blue object and the black and white bars have better spatial resolution than the red and blue bars.

The better-than-expected spatial resolution may be explained when we examine the assumption that we cannot resolve objects that are smaller than the PSF. The conclusion that we could not reconstruct objects smaller than the PSF spatial extent in the zero order made no assumptions about the radiometric shape of the PSF. In general, the PSF is close to Gaussian in the zero diffraction order. Because the PSF extent in this system covers more than one pixel, we are doing sub-PSF sampling. It is then the sub-PSF sampling effects that are contributing to the increased spatial resolution. More work in this area is needed to characterize the expected system spatial resolution.

The contrast between the peaks and valleys in both the red and blue data cubes for both objects varies significantly. When comparing the reconstructions in the red spectral bands to the reconstructions in the blue bands for Fig. 6, we see that there is greater contrast in the red bands than in the blue. Some possible causes for the variation are the

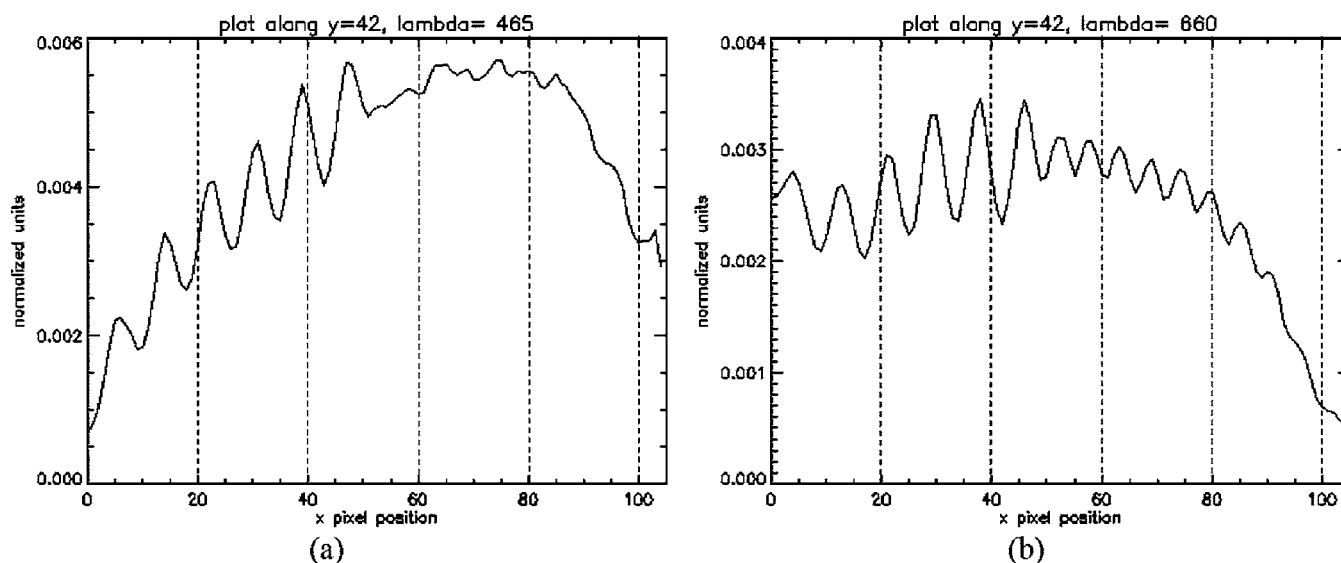


Fig. 5 Cut along a constant line of y pixels at several wavelengths of the reconstructed black and white bar data cube.

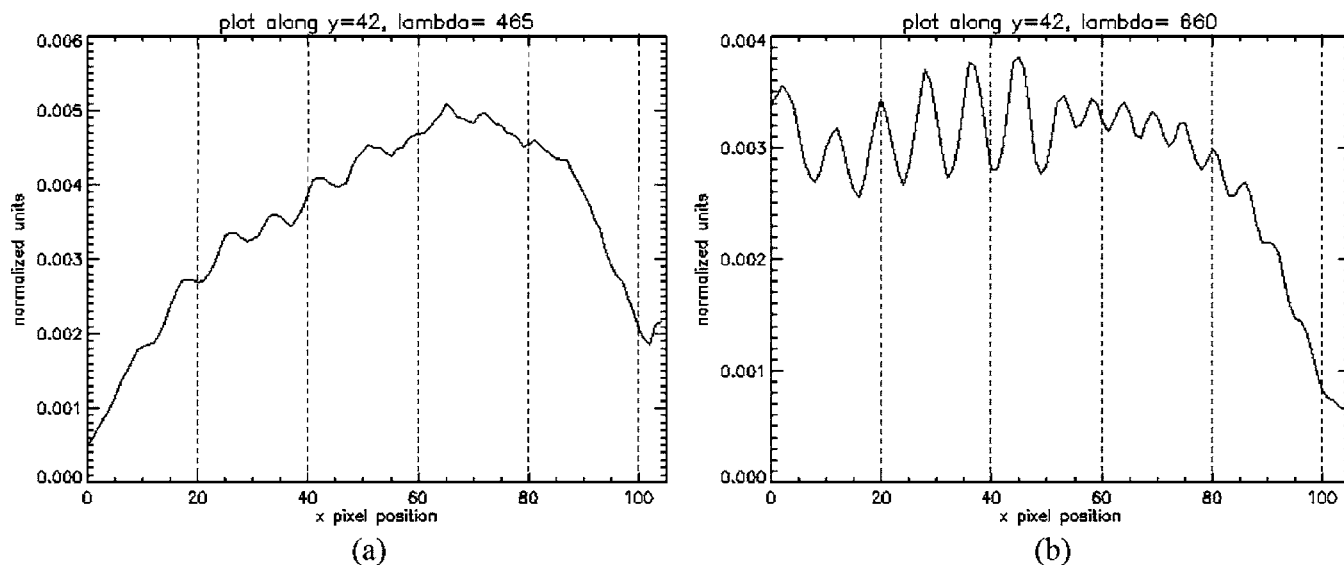


Fig. 6 Cut along a constant line of y pixels at several wavelengths of the reconstructed red and blue bar data cube.

wavelength-dependent diffraction efficiency of the CGH disperser, the responsivity of the focal plane, and the procedure used to create the system's \mathbf{H} matrix. Attempts to correlate the contribution of each cause to the measured contrast were unsuccessful and are an area of future study.

5.2 Spectral Results

To demonstrate the dual-band CTIS's ability to reconstruct the spectral signature of objects in both spectral regions, light-emitting diodes and lasers are used as objects. The spectral signature of the diodes and the laser are measured using the Ocean Optics spectrometer and compared to the CTIS reconstructed spectral signature. For the red data cube, a helium-neon laser with a center wavelength of 633 nm is shined on a white screen. For the blue data cube, we use a blue diode with a center wavelength of around 455 nm placed on a black background. For the spectral resolution, we must consider the spectral width of the object and the dispersion of the highest diffraction order. The spectral resolution is limited by the spectral line width of the calibration source and the change in wavelength over a single pixel at the highest diffraction order. The full width at half maximum spectral line width of the calibration source in this system is about 5 nm. Examining the displacement of the spots on the outer order of the calibration images, we find that a 5-nm change in the source wavelength corresponds to the center of the spot moving about 5 pixels. We can conclude that the limiting factor on the spectral resolution will be the spectral width of the calibration source. Based on the spectral line width of the source, we choose to step the wavelength of the calibration source at 5 nm. We would expect to be able to reconstruct the spectral sources to about 5 nm and resolve spectral peaks to 10 nm based on Nyquist sampling theorem.

Figure 7 shows the reconstructed spectral signature at the center of the laser spot after eight iterations of EM compared to the measured spectrum of the laser. From Fig. 7, we see that the laser spectrum was reconstructed within

the 5-nm spectral size of the voxel. With the laser peak at 633 nm, the reconstruction could have occurred in either the 630- or 635-nm bin or both. It is probable that the small spectral feature at 640 nm drew the reconstructed peak to the 635-nm bin.

Figure 8 shows the reconstructed spectrum of the blue diode compared to the measured spectrum at the center of the diode spot after eight iterations of EM. The reconstructed spectrum closely matches the measured spectrum of the diode.

The goal of the spectral reconstruction was to accurately reconstruct the spectral signature of the object with 5-nm resolution. From both the laser and the diode reconstructions, we can say that they have been accurately recon-

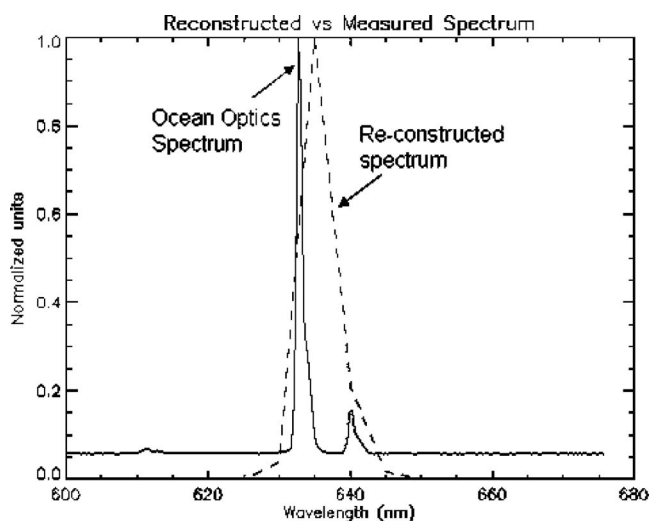


Fig. 7 Comparison of reconstructed and measured spectrum of the helium-neon laser.

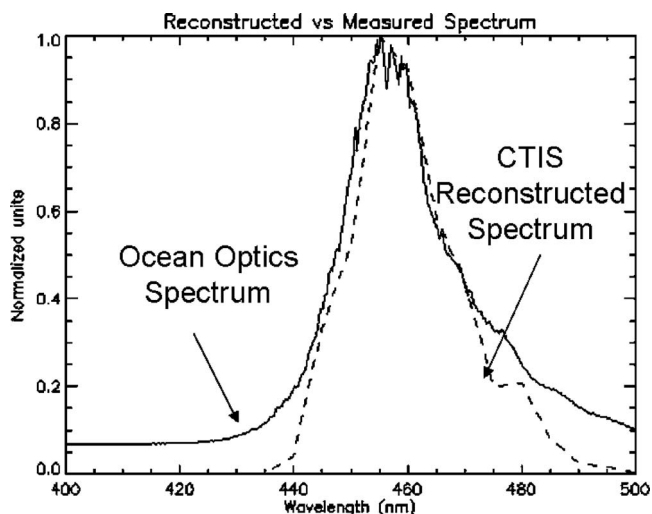


Fig. 8 Comparison between reconstructed and measured spectrum of the blue light-emitting diode.

structed, but we cannot say we have 5-nm resolution. The Nyquist sampling theorem tells us that we can do no better than 10 nm.

The laser in Fig. 7 has a spectral feature at 640 nm that was included inside the reconstructed spectral signature but was not resolved. To have a chance at resolving 5-nm features, we would have to take calibration images at 2.5-nm intervals or less. If there are two peak features that are separated by 5 nm, we would only see the valley between them if we sample between them. The spectral resolution is also impacted by the relative strength of the two spectral peaks being resolved. In the case of the laser spectrum, the 640-nm peak is too weak compared to the 633-nm peak to be recognized by the reconstruction algorithms. It is fair to conclude, based on Figs. 7 and 8, that the dual-band CTIS system under test was able to reconstruct the spectral signatures of objects in both spectral bands within 5 nm and with a 10-nm spectral resolution.

6 Conclusions

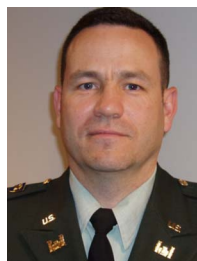
Based on this proof of concept, we can conclude that the snapshot dual-band CTIS system does allow for the reconstruction of two spatial coregistered hyperspectral data cubes. Using a camera with a focal plane consisting of detectors sensitive to two different spectral bands in an interwoven pattern makes it possible to overcome the single octave order overlap constraint inherent in spectrometers using diffraction dispersers. We are now in a position to apply this proof of concept to other portions of the spectrum. Given the emergence of dual-band infrared focal planes, our next step is to design, build, and test a dual-band hyperspectral imager in two infrared bands.

Acknowledgments

We would like to thank the United States Military Academy, the University of Arizona, and the Army Research Office for their support of this project.

References

1. A. C. Goldberg, S. W. Kennerly, J. W. Little, T. A. Shafer, C. L. Mears, H. F. Schaake, M. Winn, M. Taylor, and P. N. Uppal, "Comparison of HgCdTe and quantum-well infrared photodetector dual-band focal plane array," *Opt. Eng.* **42**(1), 30–46 (2003).
2. M. R. Descour, C. E. Volin, T. M. Gleeson, M. F. Hopkins, D. W. Wilson, and P. D. Maker, "Demonstration of a computed-tomography imaging spectrometer using a computer-generated hologram disperser," *Appl. Opt.* **36**(16), 3694–3698 (1997).
3. J. F. Scholl et al., "Phase grating design for a dual-band snapshot imaging spectrometer," *Appl. Opt.* **42**(1), 18–29 (2003).
4. G. T. Herman, *Image Reconstruction from Projections, the Fundamentals of Computerized Tomography*, Academic Press, New York (1980).
5. L. A. Shepp and Y. Vardi, "Maximum likelihood reconstruction for emission tomography," *IEEE Trans. Med. Imaging* **MI-1**(2), 113–122 (1982).
6. C. E. Volin, "Portable snapshot infrared imaging spectrometer," PhD Thesis, Univ. of Arizona, pp. 66–67 (2000).
7. A. Lent, "A convergence algorithm for maximum entropy image restoration," in *Image Analysis and Evaluation, SPSE Conference Proceedings*, Rodney Shaw, Ed., pp. 249–257 (1976).
8. C. E. Volin, "Portable snapshot infrared imaging spectrometer," PhD Thesis, Univ. of Arizona, p. 68 (2000).
9. R. Gordon, R. Bender, and G. T. Herman, "Algebraic reconstruction techniques (ART) for three-dimensional electron microscopy and X-ray photography," *J. Theor. Biol.* **29**, p. 471–481 (1970).
10. P. D. Le Van, "Perspectives on dualband infrared focal plane array efforts," *Proc. SPIE* **5563**, 130–140 (2004).



John Hartke is an Academy professor in the department of physics at the United States Military Academy, West Point, New York. He is also the research program director for the department of physics and the director of the Photonics Research Center at the Military Academy. His research interests are in hyperspectral imaging, nonlinear optical responses of optical limiters, and physics education. Dr. Hartke is a lieutenant colonel in the United States Army. He has

served as a combat engineer in a variety of operational assignments around the world including Operation Desert Storm.



Eustace L. Dereniak is a professor of optical sciences and electrical and computer engineering at the University of Arizona, Tucson, Arizona. His research interests are in the areas of detectors for optical radiation, imaging spectrometers, and imaging polarimeters instrument development. Dr. Dereniak is a coauthor of two textbooks: *Optical Radiation Detectors* and *Infrared Detectors and Systems*, both from Wiley-Interscience. He has written chapters in *Im-*

aging in Medicine, edited by S. Nudelman and Patton, related to research and development using thermograph instrumentation in the early detection of breast cancer. He has authored or coauthored over 100 refereed articles. Prior to his academic career, he spent many years in industrial research with Raytheon, Rockwell International, and Ball Brothers Research Corporation. He has served as visiting professor with the U.S. Army and Air Force, research associate with the Air Force's Rome Air Development Center, and consultant to the University of Hawaii Institute for Astronomy. He has also taught at the University of Michigan, University of New Mexico, and University of Central Florida. He is a Fellow of SPIE and the Optical Society of America and is a past member of the board of directors of SPIE. Most recently, he received the College of Optical Sciences' Annual Award of Distinction for excellence in undergraduate teaching.